






Article

Microstructure Evolution and Mechanical Behavior of TiB-Reinforced Ti-6.5Al-2Zr-1Mo-1V Matrix Composites Obtained by Vacuum Arc Melting and Spark Plasma Sintering

Maxim Ozerov ^{1,*} , Ilya Astakhov ¹ , Vitaly Sokolovsky ¹, Denis Klimenko ¹ , Nikita Stepanov ^{1,2} ,
Nikita Yurchenko ^{1,2}, Shiyao Zhao ², Lujun Huang ³ and Sergey Zharebtsov ^{1,2} 

¹ Laboratory of Bulk Nanostructured Materials, Belgorod State National Research University, 308015 Belgorod, Russia; astakhov@bsu.edu.ru (I.A.); sokolovskiy@bsu.edu.ru (V.S.); klimenko@bsu.edu.ru (D.K.); stepanov@bsu.edu.ru (N.S.); yurchenko_nikita@bsu.edu.ru (N.Y.); zharebtsov@bsu.edu.ru (S.Z.)

² World-Class Research Center “Advanced Digital Technologies”, State Marine Technical University, 198095 Saint Petersburg, Russia; 1760996@bsu.edu.ru

³ School of Materials Science and Engineering, Harbin Institute of Technology, Harbin 150001, China; huanglujun@hit.edu.cn

* Correspondence: ozerov@bsu.edu.ru; Tel.: +7-4722-58-54-16

Abstract: Ti-6.5Al-2Zr-1Mo-1V/TiB metal matrix composites with 3 wt.% of TiB₂ were obtained using vacuum arc melting and spark plasma sintering methods and compared with an unreinforced Ti-6.5Al-2Zr-1Mo-1V alloy. The microstructures of the unreinforced Ti-6.5Al-2Zr-1Mo-1V alloy in the as-cast and as-sintered conditions were quite typical and consisted of colonies of α -lamellae embedded in the β matrix. The microstructure of the as-cast Ti-6.5Al-2Zr-1Mo-1V/TiB composite composed of TiB fibers randomly distributed within the two-phase α/β matrix, while the as-sintered composite had a network-like microstructure, in which areas of the two-phase α/β matrix were delineated by walls of TiB fibers. At room temperature, the yield strength of the as-cast and as-sintered Ti-6.5Al-2Zr-1Mo-1V alloy were 800 and 915 MPa, respectively, with a plasticity of 18% in both conditions. The addition of TiB fibers contributed to a ~40 and 50% strength increment, with values of 1100 and 1370 MPa for the as-cast and as-sintered composites, respectively. In the as-sintered composite, the strengthening effect reduced at 400 °C and almost disappeared at elevated temperatures of 800–950 °C. The as-cast composite showed much higher strength during warm and hot deformation—at 800–950 °C, the yield strength of the as-cast composite was 50% higher compared to the Ti-6.5Al-2Zr-1Mo-1V unreinforced alloy. A higher rate and degree of globularization were established for the as-cast composite compared to the unreinforced alloy. For the as-sintered composite, a noticeably lower rate and degree of globularization was shown. During hot compression of the as-cast composite, TiB fibers reoriented towards the metal flow direction, while the network microstructure formed in the as-sintered composite transformed into clusters of borides unevenly distributed within the matrix. Based on the obtained results, the apparent activation energy of plastic deformation was calculated, and the operating deformation mechanisms were discussed both for the as-cast and as-sintered composites. The Arrhenius flow stress model and the dynamic material model were used to evaluate the deformation behavior of composites beyond the experimentally studied temperatures and strain rates.

Keywords: metal matrix composites; mechanical properties; microstructure; scanning electron microscopy; SEM; transmission electron microscopy; TEM



Citation: Ozerov, M.; Astakhov, I.; Sokolovsky, V.; Klimenko, D.; Stepanov, N.; Yurchenko, N.; Zhao, S.; Huang, L.; Zharebtsov, S. Microstructure Evolution and Mechanical Behavior of TiB-Reinforced Ti-6.5Al-2Zr-1Mo-1V Matrix Composites Obtained by Vacuum Arc Melting and Spark Plasma Sintering. *Metals* **2024**, *14*, 1337. <https://doi.org/10.3390/met14121337>

Academic Editor: Cristiano Fragassa

Received: 14 October 2024

Revised: 18 November 2024

Accepted: 23 November 2024

Published: 26 November 2024



Copyright: © 2024 by the authors. Licensee MDPI, Basel, Switzerland. This article is an open access article distributed under the terms and conditions of the Creative Commons Attribution (CC BY) license (<https://creativecommons.org/licenses/by/4.0/>).

1. Introduction

Titanium-based alloys are widely used in shipbuilding and aerospace industries due to their high specific strength, excellent corrosion resistance, and good manufacturability [1–3]. In addition, high-temperature titanium alloys can be used for the production of

parts operating under high-temperature conditions, such as aircraft turbine compressors. However, it should be noted that there is a noticeable decrease in strength properties at temperatures of 500–600 °C, which is mainly due to the lack of high-temperature hardening mechanisms, limiting the application of these alloys. Specifically, the operating temperatures of a well-known high-temperature near-alpha Ti-6.5Al-2Zr-1Mo-1V alloy are below 500 °C [4]. Increasing the heat resistance of titanium alloys is simultaneously a fundamental and technical problem, the solving of which opens an opportunity for these alloys to partially replace much heavier steels and nickel alloys [1–5]. Solid solution strengthening is one of the main mechanisms for strengthening titanium alloys at elevated temperatures [6]. The efficiency of this strengthening mechanism can be controlled by the chemical composition; however, the limit for titanium alloys is nearly attained. Another well-known strengthening mechanism is associated with the presence of second phases, and it can be activated by heat or thermomechanical treatment. In this case, an impressive strength up to 1500 MPa can be reached at room temperature, yet the strengthening effect disappears at 400–500 °C [6–8]. A more promising approach for improving the strength of titanium alloys at room and elevated temperatures is creating metal matrix composites (MMCs) by introducing high-strength, refractory ceramic phases into a plastic titanium matrix [9–11]. Due to its lower density and high specific strength, replacing heat-resistant alloys or steels with MMCs can lead to a reduction in the weight of structures and parts by up to 40%, which opens up extremely broad prospects for MMCs in the aerospace, automotive, and shipbuilding industries [1,2,11]. Among many options, TiB particles seem to be one of the best choices for strengthening titanium alloys: (i) these reinforcements match well with both the alpha (α)- and beta (β)-titanium matrix without the formation of a transition region; (ii) the coefficient of thermal expansion of TiB is close to that of a titanium-based matrix; and (iii) the good thermal stability of TiB can provide efficient strengthening even at elevated temperatures [11–13]. Indeed, previous studies have established a positive effect of TiB reinforcements on the high-temperature properties of some single-phase α -titanium alloys. Specifically, TiB-reinforced MMCs can be used at temperatures 100–200 °C higher in comparison to usual industrial high-temperature titanium alloys, reaching the operating temperature range of 600–800 °C [11,14]. In this interval, however, titanium-based alloys become vulnerable to oxidation or nitridation [1,2]. Therefore, the main attention must be focused on increasing strength in the temperature range up to 600 °C. At the same time, the use of thermal barrier coatings can have a significant impact on increasing the operating temperatures of titanium alloys [15–17], motivating the study of a wider temperature interval in the present work. An important factor influencing the morphology of borides and the structure of the matrix, thereby directly affecting the mechanical properties of the composites, is the method of MMC production. For example, the size of borides, which form during the casting process, can be quite large both due to the relatively slow cooling rate and hypereutectic composition of the Ti-TiB system. The formation of sufficiently large needle-like precipitates can have an impact on the reduction in the plasticity and crack resistance of MMCs [9–11]. In contrast, a short processing time and high cooling rate during spark plasma sintering (SPS) can result in the formation of much smaller (down to the nanometer range) borides [9–11,18,19]. In addition, some obvious differences in the structure can be caused by the different approach itself, i.e., powder metallurgy (SPS) and usual casting (vacuum arc melting). It should be noted that recently published works [11,18] suggest the possibility of improving the mechanical properties of titanium-based composites via thermomechanical treatment; thus, the response of the microstructure of the composites produced by different methods to hot deformation is also very interesting. Therefore, the aim of the present work was to examine the effect of the production method (casting vs. SPS) on the structure and mechanical properties of the TiB-reinforced Ti-6.5Al-2Zr-1Mo-1V alloy at room, warm, and hot deformation temperatures.

2. Materials and Methods

Laboratory versions of Ti-6.5Al-2Zr-1Mo-1V/TiB composite ingots (~60 g) were obtained by vacuum arc melting, for which metal granules of Ti, Al, Zr, Mo, and V (purity ≥ 99.9 wt.% in each case) were used with 3 wt.% of TiB₂ powder (purity 99.9%).

Vacuum arc melting was carried out in a high-purity argon atmosphere at a working temperature of 3500 °C for 60 min. The resulting ingots were remelted 5 times to obtain a uniform distribution of chemical elements throughout the volume of the blank. As a result, the ingots weighed 60 g, and no pores or other defects in the structure of the ingots were detected at the macro level. CP powders of Ti-6.5Al-2Zr-1Mo-1V (99.9% wt.%, size ~100 μm) alloy and TiB₂ (99.99% purity, size ~6 μm) were used for the sintering of the Ti-6.5Al-2Zr-1Mo-1V/TiB composite (Figure 1). A powder mixture containing 97.0 wt.% of Ti-6.5Al-2Zr-1Mo-1V and 3 wt.% of TiB₂ was obtained in a Retsch RS200 vibratory disc (RETSCH Technology, Haan, Germany) mill using ethanol as the mixing medium; the mill rotation speed was 700 rpm, and the milling time was 1 h. To prevent the mixture from heating up during milling and the particles from sticking together, milling was carried out in an ethanol environment. Ti-6.5Al-2Zr-1Mo-1V/TiB composite specimens having a cylindrical form with dimensions of 25 (height) \times 19 (diameter) mm were synthesized by the SPS process in high vacuum using a Thermal Technology SPS 10-3 machine; the synthesis temperature was 1500 °C at a pressure of 40 MPa for 15 min. The residual porosity was estimated by the hydrostatic weighing method using automatic standard porosimeter Porotech 3.1, as well as metallographic analysis; as a result, the porosity values measured by the two methods did not exceed 0.5%. The measured density was 4.806 g/cm³. For the sake of comparison, unreinforced (i.e., without the addition of TiB₂) Ti-6.5Al-2Zr-1Mo-1V alloy specimens were also fabricated using vacuum arc melting and SPS. The labeling of the materials investigated is presented in Table 1.

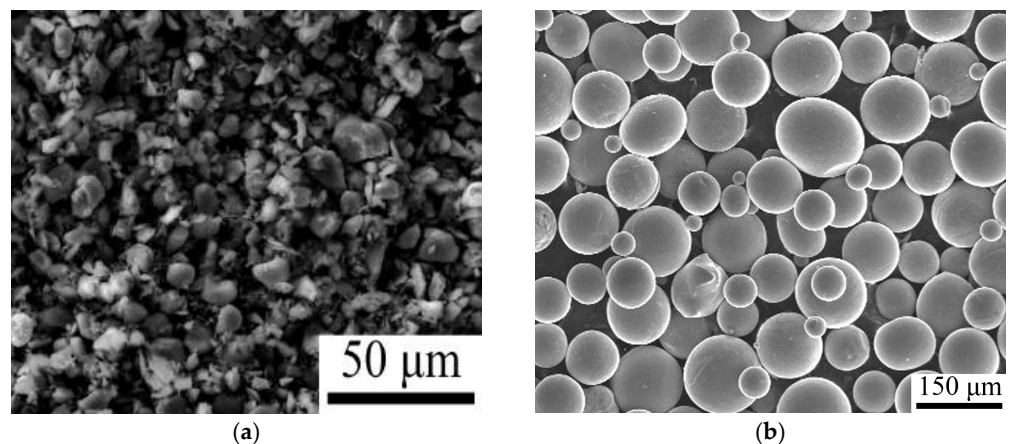


Figure 1. SEM images of TiB₂ (a) and Ti-6.5Al-2Zr-1Mo-1V (b) powders.

Table 1. Designation of the materials studied.

Condition	Marking
Ti-6.5Al-2Zr-1Mo-1V alloy produced by vacuum arc melting	AC-Alloy
Ti-6.5Al-2Zr-1Mo-1V/TiB composite produced by vacuum arc melting	AC-Composite
Ti-6.5Al-2Zr-1Mo-1V alloy produced by spark plasma sintering	SPS-Alloy
Ti-6.5Al-2Zr-1Mo-1V/TiB composite produced by spark plasma sintering	SPS-Composite

Specimens measuring $4 \times 4 \times 6$ mm³ were cut from the produced materials using a Sodick AQ300L electro-discharge machine (Sodick Inc., Schaumburg, IL, USA). Then, the specimens were isothermally compressed in air at 20, 400, 600, 800, 900, and 950 °C at a nominal strain rate of 10^{-3} s⁻¹ by 50% height reduction using an Instron 300LX

testing machine. The compression tests with deformation change were carried out at deformation rates of 10^{-2} , 5×10^{-3} , 10^{-3} , and $5 \times 10^{-4} \text{ s}^{-1}$, and the temperature range was 750–950 °C. After that, the values of the plastic deformation activation energy for the alloys and composites were calculated. The microstructures of the initial and deformed specimens were investigated using a FEI Quanta 600 (Thermo Fisher Scientific, Hillsboro, OR, USA) and Tescan Mira 3 (Tescan, Brno, Czech Republic) scanning electron microscope (SEM) in backscattered electron (BSE) and secondary electron (SE) regimes. The specimens for SEM were prepared by careful mechanical polishing; to reveal borides in the structure of the composites (for SE regime), deep etching (for ~5 min) was carried out using the Kroll's reagent (95% H₂O, 3% HNO₃, 2% HF). The samples for transmission electron microscopy (TEM) were first mechanically thinned to ~100 μm and then electrolytically polished at −35 °C and 29 V using a mixture of 60 mL perchloric acid, 600 mL methanol, and 360 mL butanol. The resulting thin foils were examined using a JEOL JEM 2100 (JEOL, Tokyo, Japan) transmission electron microscope. The linear intercept method was used to quantify the average length or diameter of the boride fibers and fraction of globular particles. For calculation by this method, Digimizer software version 4.3.0 (MedCalc Software Ltd., Ostend, Belgium) was used. For each condition, at least 500 measurements were carried out.

To evaluate the deformation behavior of composites beyond the experimentally studied temperatures and strain rates, the Arrhenius flow stress model and the dynamic material model (DMM) were used. The constitutive equation is represented by a mathematical model that shows the relationship between the flow stresses and hot deformation parameters of deformed alloys. The Arrhenius model was used to predict the behavior of AC and SPS composites during hot deformation. The equation can be expressed in the following form (Equation (1)):

$$\dot{\varepsilon} = AF(\sigma) \exp\left(\frac{-Q}{RT}\right) \quad (1)$$

where $F(\sigma)$ is a function of the flow stress and can be expressed as:

$$\begin{cases} F(\sigma) = \sigma^{n_1}, (\alpha\sigma < 0.8) \\ F(\sigma) = \exp(\beta\sigma), (\alpha\sigma > 1.2) \\ F(\sigma) = [\sinh(\alpha\sigma)]^n, (\text{for all } \sigma) \end{cases} \quad (2)$$

where $\dot{\varepsilon} (\text{s}^{-1})$ is the strain rate; Q (KJ/mol) is the hot activation energy; T (K) is the deformation temperature; R ($8.314 \text{ J} \cdot \text{mol}^{-1} \cdot \text{K}^{-1}$) is the gas constant; σ (MPa) is the flow stress; and A , n_1 , β , α ($\alpha = \beta/n_1$), and n are material constants. The power law equation and exponential law equation are suitable for low-stress ($\alpha\sigma < 0.8$) and high-stress ($\alpha\sigma > 1.2$) deformation, respectively.

Taking Equation (2) into Equation (1) and taking the logarithm of both ends of the equation, the following is obtained:

$$\begin{cases} \ln(\sigma) = \frac{1}{n_1} \ln(\dot{\varepsilon}) + \frac{1}{n_1} \left(\frac{Q}{RT} - \ln(A) \right), (\alpha\sigma < 0.8) \\ \sigma = \frac{1}{\beta} \ln(\dot{\varepsilon}) + \frac{1}{\beta} \left(\frac{Q}{RT} - \ln(A) \right), (\alpha\sigma > 1.2) \\ \ln[\sinh(\alpha\sigma)] = \frac{1}{n} \ln(\dot{\varepsilon}) - \frac{1}{n} \ln(A) + \frac{Q}{nRT}, (\text{for all } \sigma) \end{cases} \quad (3)$$

Based on the relationship diagrams $\ln(\sigma) - \ln(\dot{\varepsilon})$, $\sigma - \ln(\dot{\varepsilon})$, and $\ln[\sinh(\alpha\sigma)] - \ln(\dot{\varepsilon})$, the n_1 , β , and n were obtained from the reciprocal of the slope of the corresponding curve. Then, the value α was calculated as $\alpha = \beta/n_1$. Furthermore, the slope and intercept of $\ln[\sinh(\alpha\sigma)] - 1000/T$ were the values of Q/nR and $(\ln(\dot{\varepsilon}) - \ln(A))/n$, and then the values of Q and $\ln(A)$ were calculated.

In addition, the Z parameter proposed by Zener and Hollomon can express the relationship between the strain rate and deformation temperature as follows [20].

$$Z = \dot{\varepsilon} \exp\left(\frac{Q}{RT}\right) = A[\sinh(\alpha\sigma)]^n \quad (4)$$

Depending on the definition of the hyperbolic law, the flow stress with the Z parameter can be given as:

$$\sigma = \frac{1}{\alpha} \ln \left\{ \left(\frac{Z}{A} \right)^{\frac{1}{n}} + \left[\left(\frac{Z}{A} \right)^{\frac{2}{n}} + 1 \right]^{\frac{1}{2}} \right\} \quad (5)$$

The root mean square deviation (RMSE) was used to assess the accuracy of the model's forecast.

$$RMSE = \sqrt{\frac{1}{n} \sum_{i=1}^n (\sigma(YSP)_i - \sigma(YSE)_i)^2} \quad (6)$$

where $\sigma(YSE)_i$ and $\sigma(YSP)_i$ are the experimental and predicted yield strength for a given temperature and strain rate, respectively.

Strain-corrected values α , n , Q , and $\ln(A)$ were tuned by using the genetic algorithm. Genetic algorithms are classes of algorithms inspired by the process of natural selection [21]. In this case, the genotype of each individual was composed of 4 values— α , n , Q and $\ln(A)$ [22]. Several individuals formed a population (generation), and we used a generation with 2000 individuals. For each individual in a generation, a fitness function was calculated, and some individuals with the highest fitness values (parents) were selected to generate a next population (selection). The RMSE was used as a fitness function, and 15 individuals in each generation were selected as parents. For each possible pair of parents (106 possible variants), six individuals of the next generation were created by crossovers after the first, second, and third gens. From each of the obtained individuals, by mutation (changing the value to a random one) in one random gene, one more individual of the next generation was formed. After removing duplicate individuals, the generation was supplemented with randomly generated individuals up to a specified number. After 100 generations, the average value for each parameter was obtained for 15 individuals with the best fitness function values. The obtained values of the parameters α , n , Q , and $\ln(A)$ were interpolated by a 5th-degree polynomial:

$$F(e) = k_5 e^5 + k_4 e^4 + k_3 e^3 + k_2 e^2 + k_1 e + k_0 \quad (7)$$

where e is strain and k_i is the coefficient of the corresponding degree.

To evaluate the machinability of alloys, the DMM proposed by Prasad et al. [23] was used. The hot process diagram was produced by superimposing the power dissipation efficiency and instability diagrams. The power dissipation efficiency (η) was defined as the ratio of the power consumed by the microstructure evolution to the total power, as follows:

$$\eta = \frac{2m}{m+1} \quad (8)$$

where m is the strain rate sensitivity index, as follows:

$$m = \frac{\delta \ln(\sigma)}{\delta \ln(\dot{\epsilon})} \quad (9)$$

The value of η is high when flow instability (e.g., microcracks, adiabatic shear bands, and flow localization) occurs. Therefore, it is necessary to combine the instability criterion to prove the machinability of the alloy [24]:

$$\zeta(\dot{\epsilon}) = \frac{\delta \ln \left[\frac{m}{m+1} \right]}{\delta \ln(\dot{\epsilon})} + m \quad (10)$$

when $\zeta(\dot{\epsilon})$ is less than 0, flow instability will occur during the deformation process.

3. Results

3.1. Initial Microstructure

The initial microstructure of the unreinforced Ti-6.5Al-2Zr-1Mo-1V alloys in the as-cast and as-sintered (i.e., produced by SPS) conditions was quite typical and consisted of colonies of α -lamellae in the β matrix (Figure 2). In both conditions, the size of initial β -grains and α -colonies were found to be ~ 2 – 2.5 mm and ~ 100 – 150 μm , respectively.

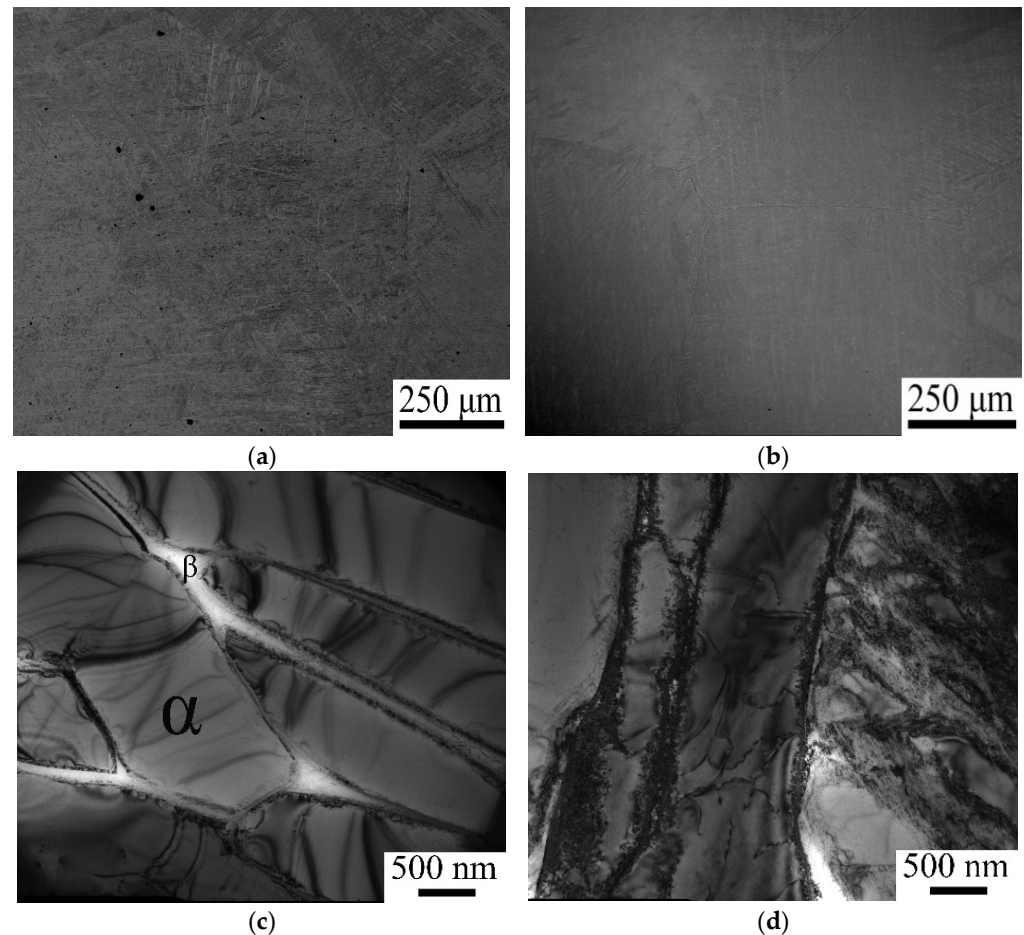


Figure 2. Initial microstructure the AC-Alloy (a,c) and SPS-Alloy (b,d): (a,b)—SEM-BSE images; (c,d)—TEM images.

In contrast, the microstructure of the AC-Composite and SPS-Composite differed from each other noticeably (Figure 3). Specifically, the AC-Composite consisted of TiB fibers randomly distributed within the two-phase α/β matrix (Figures 3a–c and 4a). The average space between the TiB particles was ~ 25 μm ; the average size of the α -colonies was ~ 60 μm (Figure 3b,c). The α -lamellae thickness and the thickness of the β -layer were ~ 800 nm and ~ 150 nm, respectively (Figure 3b,c). The volume fraction of the β -phase was $\sim 6\%$. Meanwhile, the SPS-Composite had a network-like microstructure (Figure 3d,e). There were areas of the two-phase α/β matrix (~ 90 μm diameter) that were delineated by walls of TiB particles (Figures 3d,e and 4b). A similar structure was obtained in [18,25] using low-energy ball milling and subsequent hot isotactic pressure. The average size of the α -colonies was similar to that of the AC-Composite, viz. ~ 40 μm . The average thickness of the α -lamellae and the β -layer were ~ 1 μm and ~ 500 nm, respectively (Figure 3e,f). In the case of the AC-Composite, the volume fraction of the β -phase was $\sim 6\%$. In both the AC-Composite and SPS-Composite, the TiB fibers had a prismatic cross-section with the faces created by the (100), (101), and (10–1) planes [19]. The values of the average length and cross-sectional size of the TiB fibers in the AC-Composite structure were ~ 26 μm and

$\sim 2.6 \mu\text{m}$, respectively. (Figure 3b,c). These dimensions were slightly lower ($\sim 18 \mu\text{m}$ and $\sim 2.3 \mu\text{m}$, respectively) in the SPS-Composite (Figure 3e,f). The volume fractions of TiB were found to be $\sim 10\%$ and 6% in the AC-Composite and SPS-Composite, respectively (Figure 3b,e); this difference can be associated with stereology since a two-dimensional section underestimates the volume fraction for a three-dimensional distribution of the TiB particles because mainly the perpendicular (with respect to the section) walls of the network architecture can be seen.

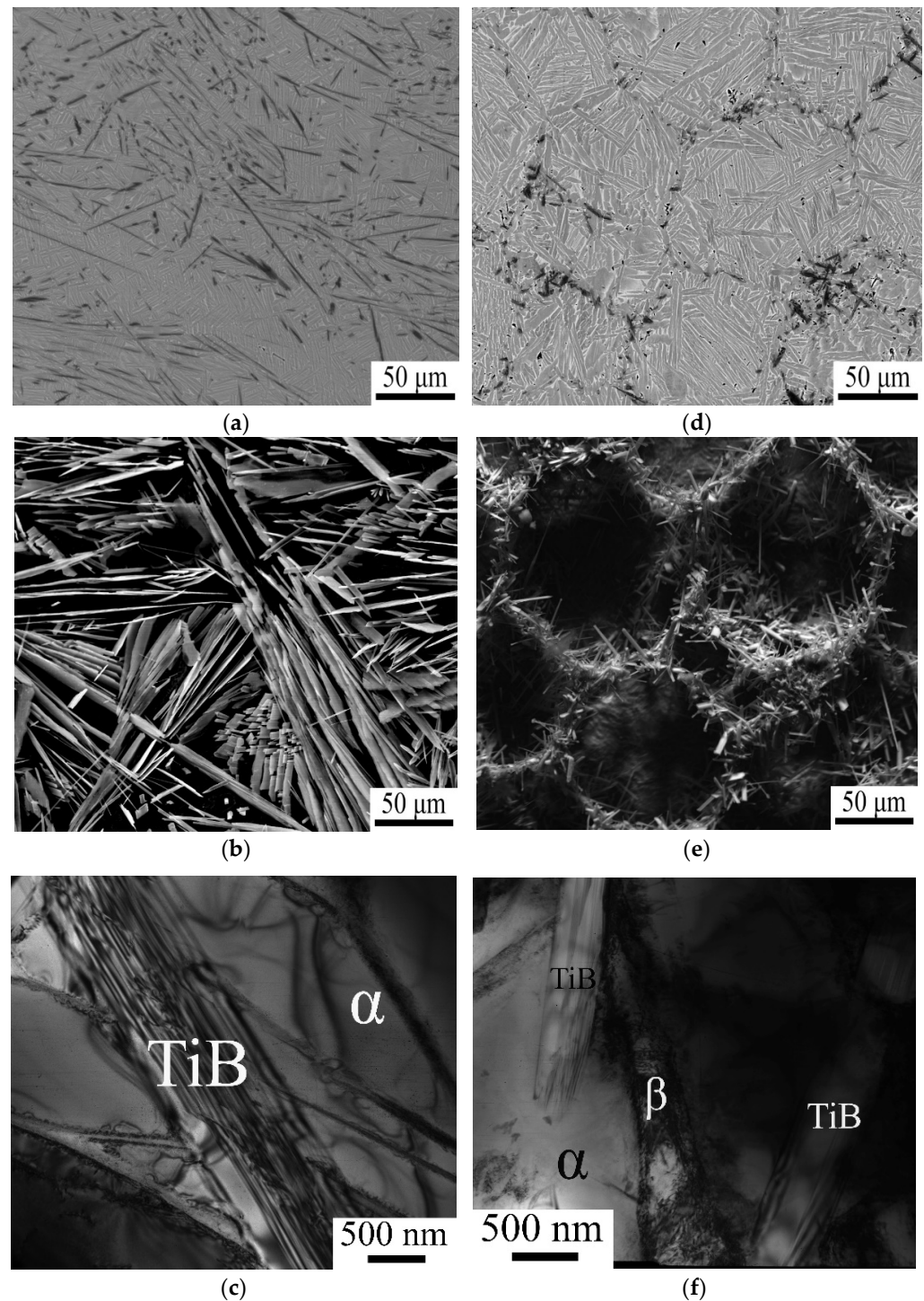


Figure 3. Initial microstructure of the AC-Composite (a–c) and SPS-Composite (d–f): (a,d)—SEM-BSE images; (b,e)—SEM-SE images of the etched surfaces; and (c,f)—TEM images.

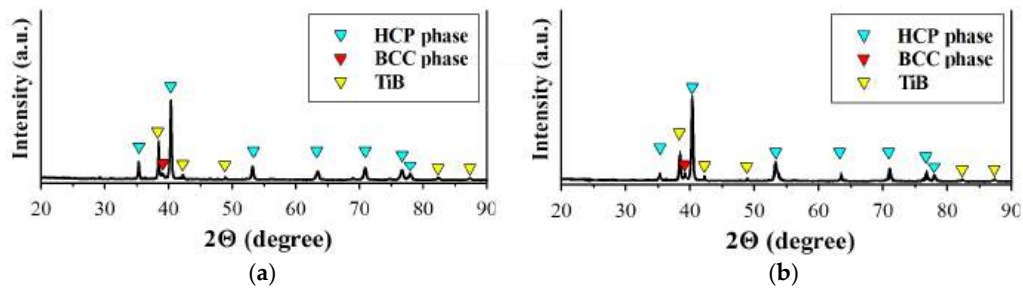


Figure 4. XRD patterns of the AC-Composite (a) and SPS-Composite (b).

3.2. Mechanical Properties

The addition of TiB reinforcements resulted in a significant increase in strength in compression (irrespective of the production method) compared to the unreinforced alloy (Figures 5 and 6, Table 2). For example, at room temperature, the AC-Composite was found to be ~40% stronger than the AC-Alloy. Similarly, the SPS-Composite had a ~50% higher strength than the SPS-Alloy. Note that in the SPS-Composite, the strengthening effect reduced during warm deformation (400 °C) and almost disappeared at elevated temperatures (800–950 °C) (Figures 5 and 6, Table 2). Meanwhile, the AC-Composite showed a much higher strength during warm and hot deformation. For example, at 950 °C, the yield strength of the AC-Composite doubled that of the AC-Alloy (Figure 6, Table 2). In addition, the compression tests suggested higher strength values of the SPS-Composite in comparison to those of the AC-Composite at room temperature and 400 °C (Figure 5, Table 2). However, at 600 °C, this difference disappeared, and, at higher temperatures, the AC-Composite became stronger (Figures 5 and 6, Table 2). Note that the AC-Alloy and SPS-Alloy also followed the above-mentioned trend during deformation at different temperatures.

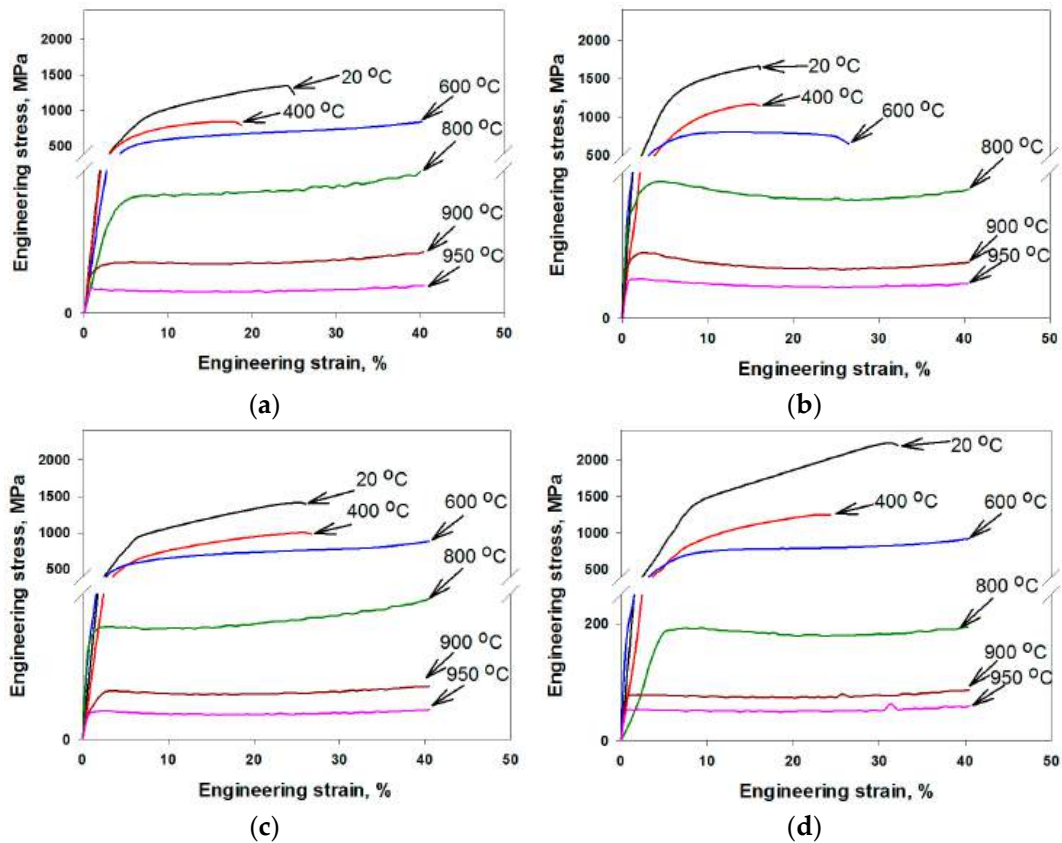


Figure 5. Engineering stress–strain curves obtained during compression at 20–950 °C: (a)—AC-Alloy; (b)—AC-Composite; (c)—SPS-Alloy; and (d)—SPS-Composite.

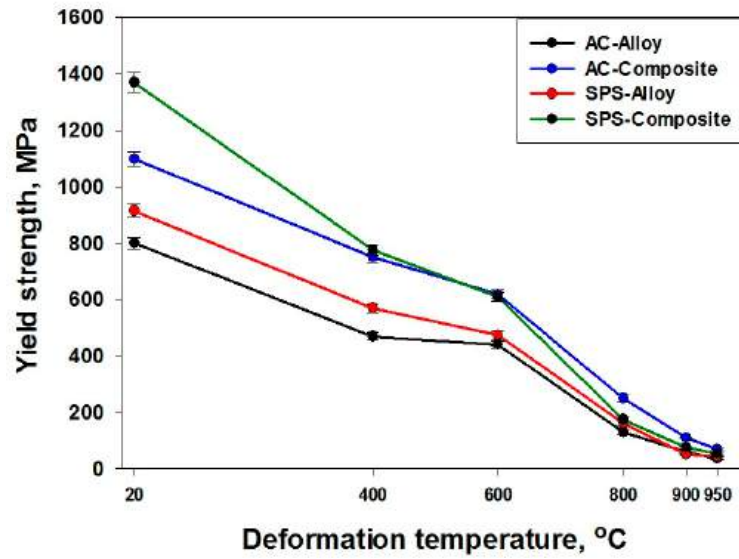


Figure 6. Yield strength of the AC-Alloy, AC-Composite, SPS-Alloy, and SPS-Composite as a function of temperature in the range of 20–950 °C.

Table 2. Compression yield strength of the AC-Alloy, AC-Composite, SPS-Alloy, and SPS-Composite at various deformation temperatures.

Compression Temperature, °C	Yield Strength, MPa			
	AC-Alloy	AC-Composite	SPS-Alloy	SPS-Composite
20	800 ± 20	1100 ± 25	915 ± 24	1370 ± 35
400	470 ± 14	750 ± 18	570 ± 16	775 ± 19
600	440 ± 14	620 ± 16	475 ± 15	610 ± 16
800	130 ± 7	250 ± 10	160 ± 8	175 ± 9
900	60 ± 4	110 ± 5	50 ± 3	75 ± 5
950	35 ± 2	70 ± 4	44 ± 2	55 ± 3

3.3. Constitutive Model with Compensation of Strain and Processing Map

Based on the relationship diagrams, the n_1 , β , n , α , Q , and $\ln(A)$ were calculated for both composites. The Supplementary Materials provide the corresponding graphs for the AC-Composite (Figure S1) and the SPS-Composite (Figure S2). For the AC-Composite, the following values were obtained: $n_1 = 5.1890$, $\beta = 0.0237$, $\alpha = 0.0046$, $n = 3.4855$, $Q = 394$, and $\ln(A) = 34.1134$. For the SPS-Composite, the respective values were: $n_1 = 4.6105$, $\beta = 0.0256$, $\alpha = 0.0055$, $n = 3.1325$, $Q = 348$, and $\ln(A) = 30.3642$.

The values obtained were used to calculate the yield strength values during the strain rate jump compression tests. Figure 7 shows the comparison between the experimental and predicted values of yield strength for the AC-Composite (Figure 7a) and the SPS-Composite (Figure 7b). Evidently, the model predicts yield strengths well for the SPS-Composite (RMSE = 8.3 MPa), while for the AC-Composite (RMSE = 54 MPa), the agreement between the predicted and experimental values is worse.

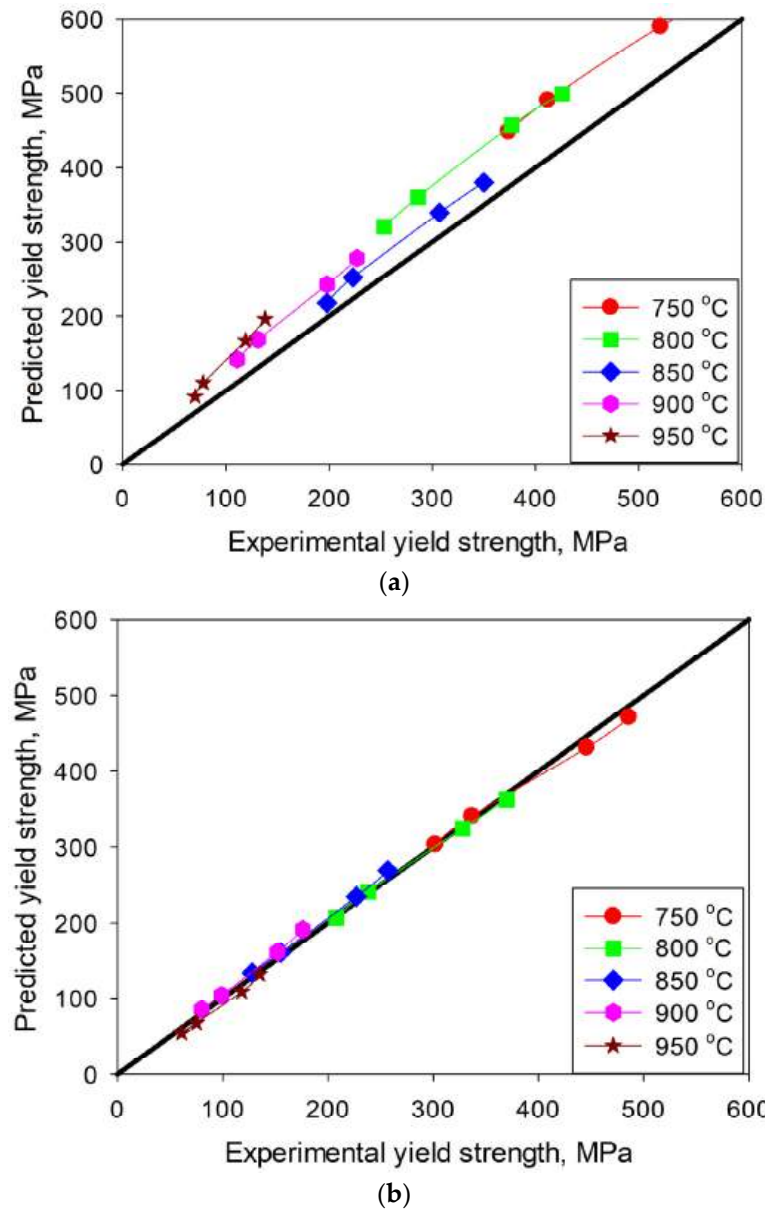


Figure 7. The graph of the correspondence between the experimental and predicted values of the yield strength at strain rates of 10^{-2} , 5×10^{-3} , 10^{-3} , and $5 \times 10^{-4} \text{ s}^{-1}$ in the temperature interval of 1023–1223 K for the AC-Composite (a) and the SPS-Composite (b).

The obtained parameters (α , n , Q , and A) do not allow for calculating the stress–strain dependencies. Based on engineering curves for the strain rate of 0.001 and temperatures of 600–950 °C (Figure 5) for the AC- and SPS-Composites, the parameters α , n , Q , and $\ln(A)$ were tuned using genetic algorithms to ensure the best agreement with the experimental values. Strain-corrected values were calculated for strain 0.05–0.4 (with step 0.05). The graphs of the dependence of the parameters α , n , Q , and $\ln(A)$ on the deformation for the AC-Composite (Figure S3) and the SPS-Composite (Figure S4), as well as the coefficients of the equations for them (Table S1), are given in the Supplementary Materials. True stress–true strain curves based on strain-dependence α , n , Q , and A are shown for the AC-Composite (Figure 8a) and the SPS-Composite (Figure 8b).

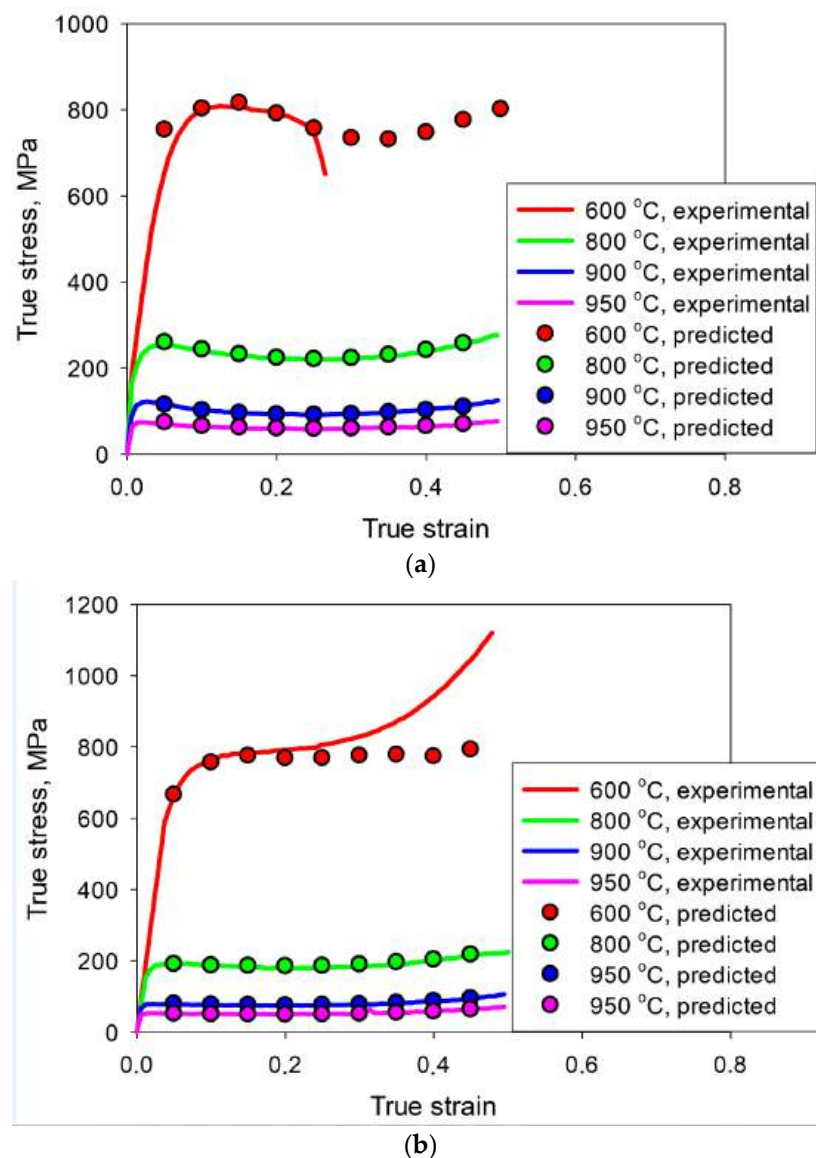


Figure 8. Experimental and calculated true strain–true stress curves for the AC-Composite (a) and SPS-Composite (b).

As can be seen from the presented graphs, the calculated stress values showed good agreement with the experimental data. Using this model, the deformation curves were calculated in the temperature range of 600–950 °C and strain rates of 0.5–0.0001 s⁻¹. Based on the calculated engineering curves constructed for a wide range of deformation rates and temperatures, processing maps for different strains were constructed for both types of composites (Figure S5).

It can be noted that both the SPS-Composite and the AC-Composite were characterized by the presence of a region of unstable flow at high strain rates and low temperatures. However, for the AC-Composite, the region of unstable flow expanded to higher temperatures. With increasing strain, the region of unstable flow for both composites changed insignificantly. For the AC-Composite, with increasing strain, there was an insignificant shift of the regions of low power dissipation efficiency and high power dissipation efficiency to the center of the graph. For the SPS-Composite, with increasing strain, there was a decrease in the power dissipation efficiency. In general, the SPS-Composite shows higher values of η compared to the AC-Composite.

3.4. Microstructure Evolution During Deformation SEM Observation

Because of limited plasticity (even at 600 °C, the AC-Composite failed at a strain of less than 25%), the microstructure evolution of the materials was studied at 800 °C. Depending on the initial spatial orientation of the α -phase particles, the microstructure evolution of the AC-Alloy during deformation in the range of 800–950 °C was associated either with the alignment of the α -lamellae along the metal flow direction or with globularization (Figure 9a–c). It should be noted that the globularization kinetics intensified with increasing temperature (Figure 9a).

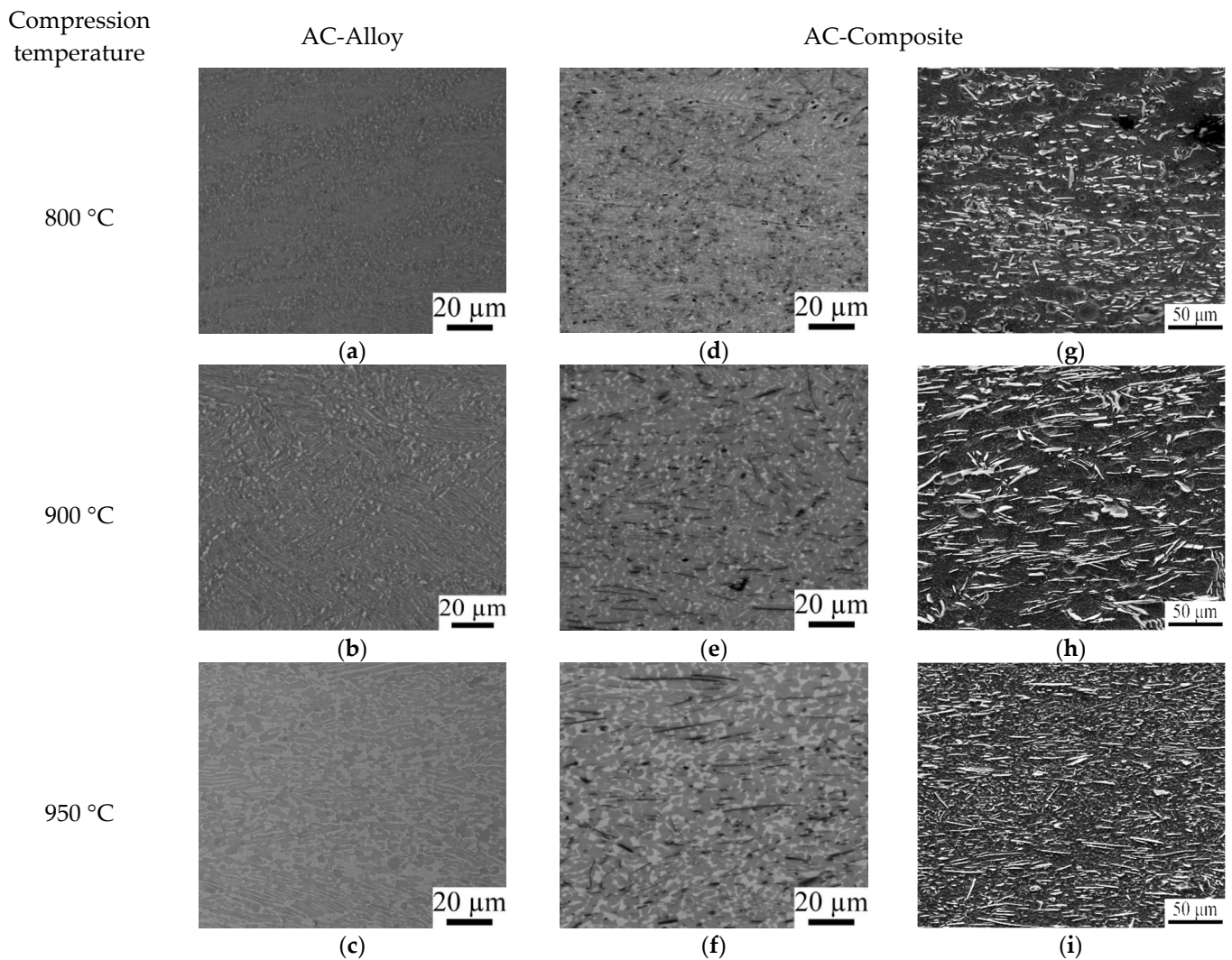


Figure 9. SEM images of the microstructure of the AC-Alloy (a–c) and AC-Composite (d–i) after compression at 800 (a,d,g), 900 (b,e,h), and 950 °C (c,f,i): (a–f)—SEM-BSE images and (g–i)—SEM-SE images of the etched surfaces.

The microstructure evolution of the AC-Composite was not qualitatively different from that observed in the AC-Alloy (Figures 9d–f and 10). However, a higher rate of globularization can be noticed (Figure 11a). Due to this, after hot deformation, a much more uniform microstructure was formed in the structure of the AC-Composite. It was also shown that the fraction of the globularized structure increased with increasing deformation temperature in the interval of 800–950 °C from ~40 to ~80% in the AC-Alloy and from ~55 to ~90% in the AC-Composite. The average size of the α -particles in the AC-Alloy and AC-Composite were practically the same; for example, after deformation at 950 °C,

the average size of the α -particles was $2.5 \pm 0.5 \mu\text{m}$ and $3.2 \pm 0.5 \mu\text{m}$ for the AC-Alloy and AC-Composite, respectively. With increasing deformation temperature to $950 \text{ }^\circ\text{C}$, the volume fraction of the β -phase increased to 30 vol.% in the AC-Alloy and to 15 vol.% in the AC-Composite.

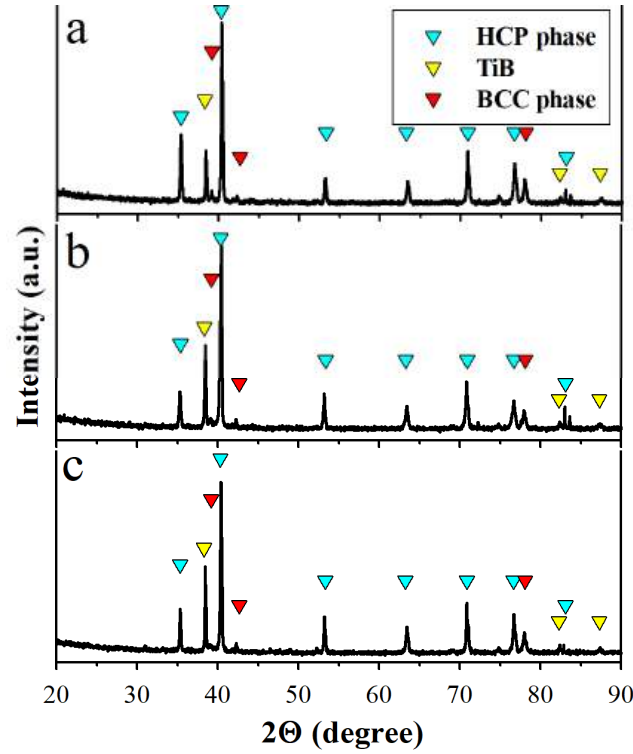


Figure 10. XRD patterns of the AC-Composite after compression at 800 (a), 900 (b), and 950 (c) $^\circ\text{C}$.

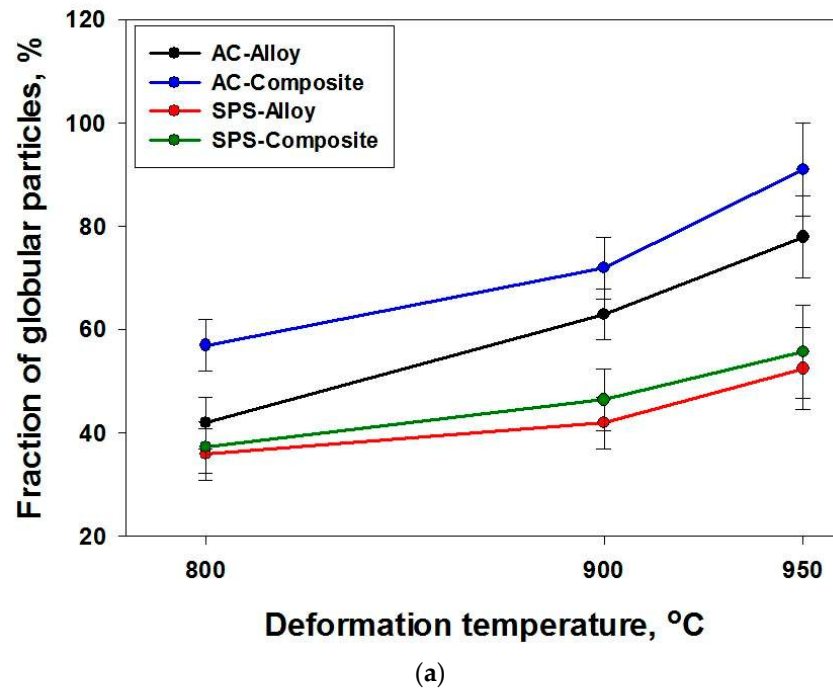


Figure 11. Cont.

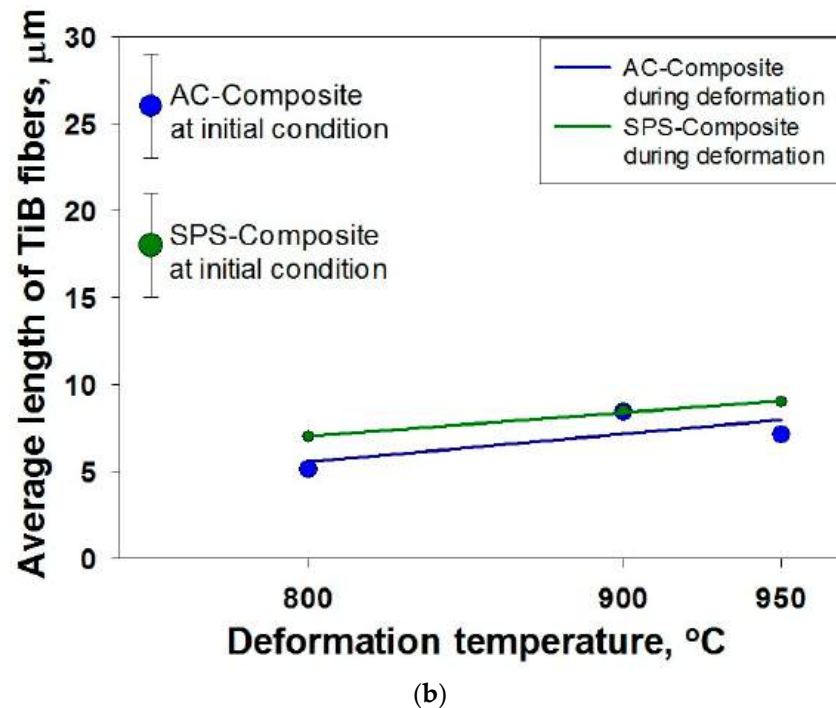


Figure 11. Values of the proportion of globular particles during deformation at 800–950 °C (a) and the apparent length of TiB fibers in the structure of the AC-Composite and SPS-Composite (b).

During the uniaxial hot compression of the composite, TiB fibers reoriented towards the metal flow direction (Figure 9g–i). A significant shortening of the TiB fibers from ~25 μm in the initial structure to ~5–7 μm after hot compression should also be noted (Figures 9 and 11b). The average diameter of the TiB fibers decreased to ~0.8 μm (in comparison to the initial value of ~2.6 μm) as a result of deformation. Hot deformation decreased the length-to-diameter ratio to $l/d \leq 10$, due to which the contribution of the Orowan hardening mechanism became dominant [26].

The main qualitative difference in the microstructure evolution during hot deformation of the as-cast and as-sintered states was a noticeably lower rate of globularization of the α -lamellae (Figures 12 and 13). This trend was typical for both the SPS-Alloy and SPS-Composite. In addition, a less pronounced increase in the fraction of globularized particles in the structure of the composite with increasing deformation temperature should be noted; for the as-sintered condition, the volume fraction of globular α increased from ~37 to ~52% in the unreinforced alloy and from ~37 to ~56% in the composite (Figures 9, 11a and 12).

There were also significant differences in the behavior of borides during deformation in comparison to that obtained in the AC-Composite. The network microstructure formed in the SPS-Composite (Figure 3d,e) transformed into clusters of borides unevenly distributed within the matrix (Figure 9g–i). The shortening of TiB fibers was less intensive compared to that of the AC-Composite (Figure 11b). Thus, an irregular distribution of TiB fibers and their less intense shortening could have a direct effect on the strength properties of the SPS-Composite in the temperature range of 800–950 °C (Figures 5 and 6).

TEM analysis of the materials studied after deformation at 800–950 °C showed no noticeable effect of the production method on microstructure evolution. New recrystallized grains could already be observed in the microstructure of each studied condition at 800 °C (as an example, the AC-Alloy and AC-Composite structures are shown in Figure 14a–d). The intensity of dynamic recrystallization expectedly increased with temperature. Similar to the result of the SEM investigation, more pronounced globularization could be suggested in the composites in comparison to that of unreinforced alloy, so that even at 950 °C, β -lamellae were observed in the AC-Alloy (Figure 14c), while a mainly globular microstructure was formed in the AC-Composite (Figure 14d).

In turn, both the SPS-Alloy and SPS-Composite demonstrated a lower inclination to dynamic globularization in comparison to the as-cast condition, thereby also confirming the result of SEM (Figures 9 and 12). Specifically, the SPS-Alloy demonstrated an almost intact lamellar microstructure with only isolated recrystallized grains even after deformation at 900 °C (Figure 15a). An increase in deformation temperature to 950 °C resulted in a more complete globularization (Figure 15b).

The presence of the TiB reinforcements had a minor effect on microstructure evolution near the particles. The interphase boundary was found to be clear without redundant dislocation density. However, in some cases, the formation of dislocation walls or subgrains could be observed in the vicinity of the particles (Figure 16a,b).

Compression temperature

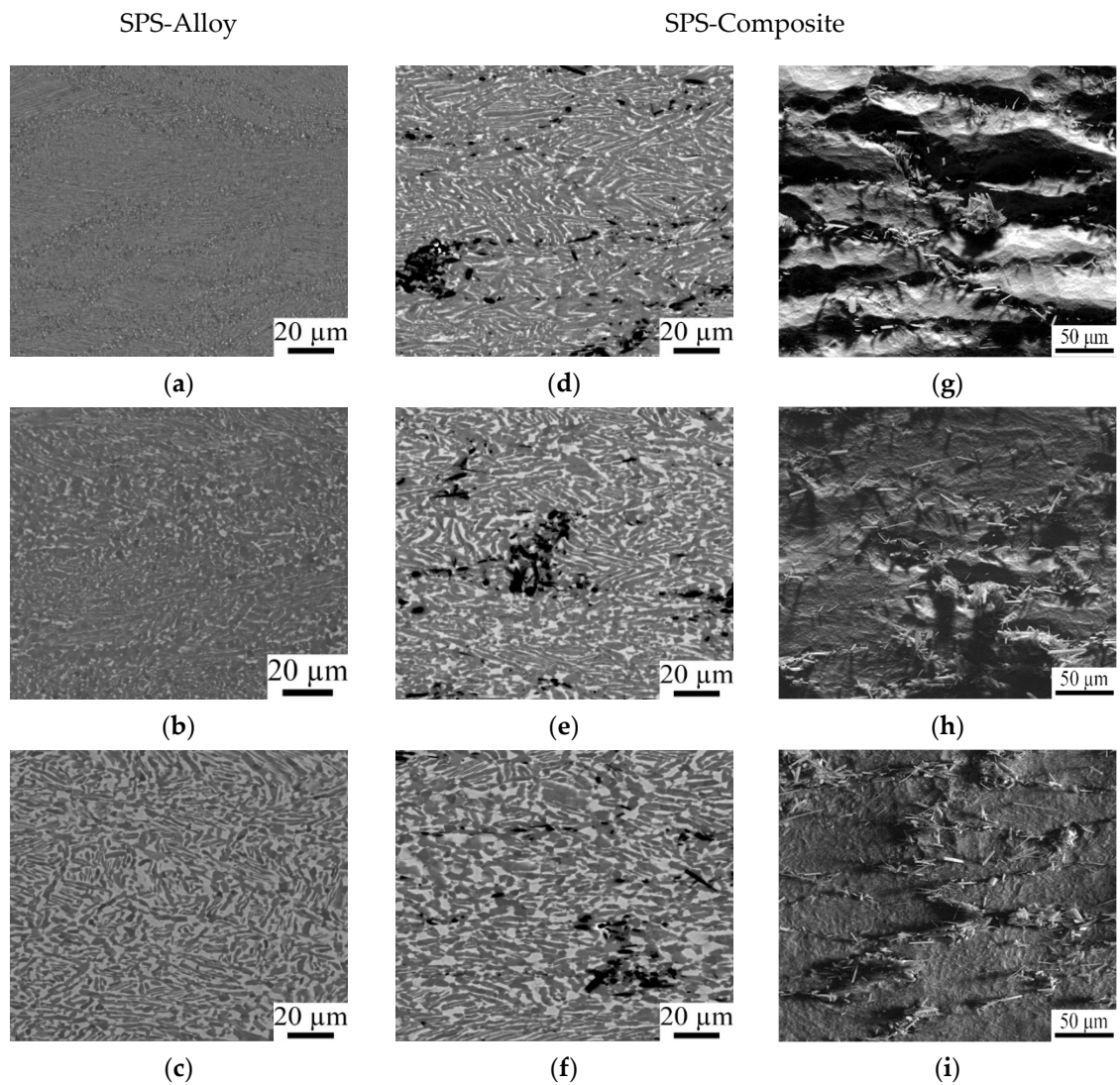


Figure 12. SEM images of the microstructure of the SPS-Alloy (a–c) and SPS-Composite (d–i) after compression at 800 (a,d,g), 900 (b,e,h), and 950 °C (c,f,i): (a–f)—SEM-BSE images and (g–i)—SEM-SE images of the etched surfaces.

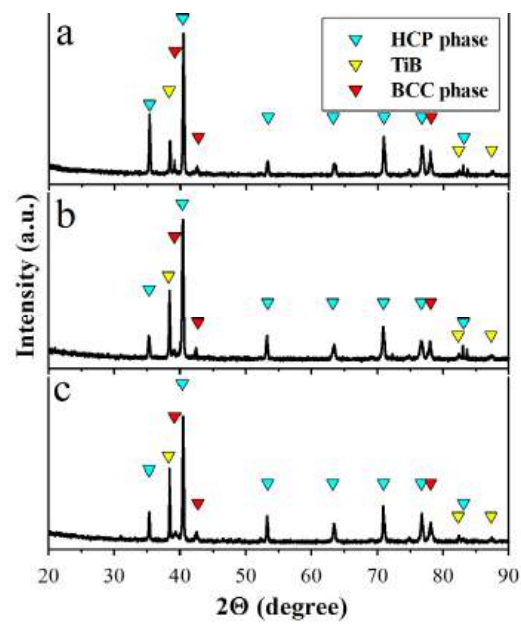


Figure 13. XRD patterns of the SPS-Composite after compression at 800 (a), 900 (b), and 950 (c) °C.

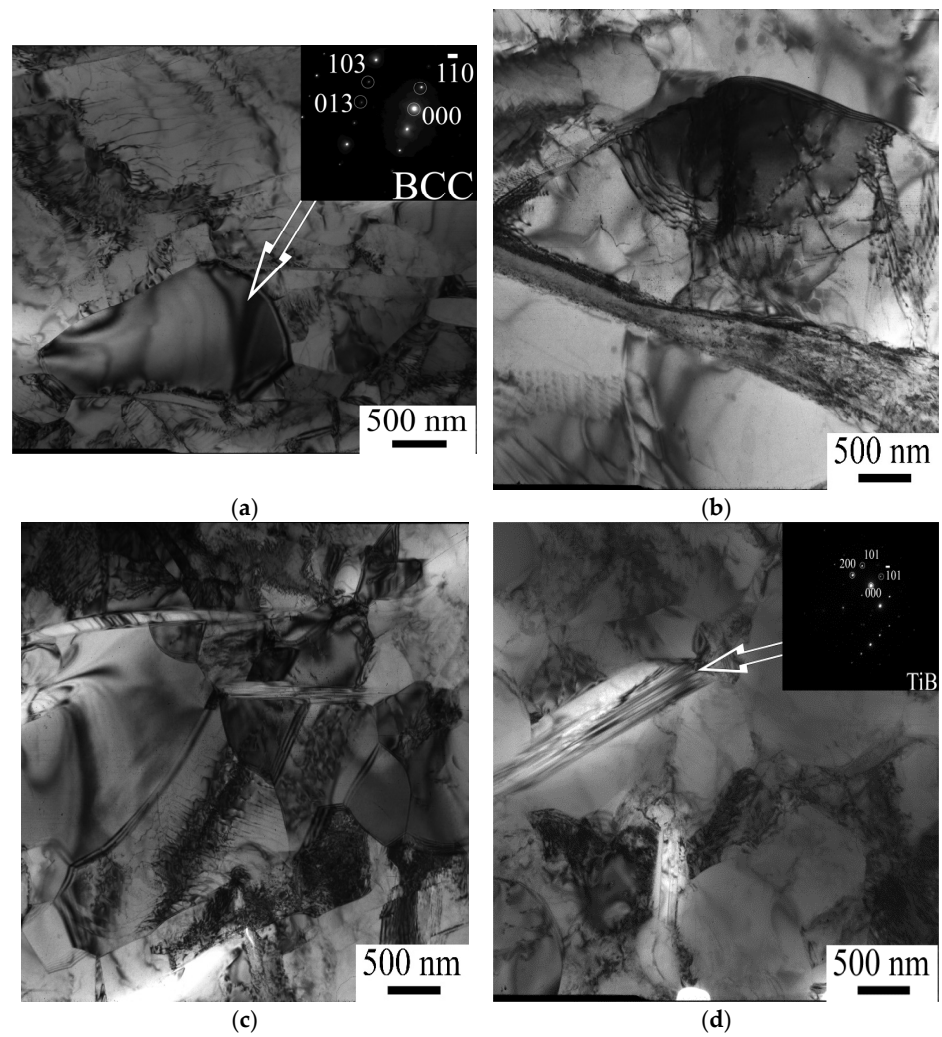


Figure 14. TEM images of the AC-Alloy (a,b) and AC-Composite (c,d) after deformation at 800 °C (a,c) or 950 °C (b,d).

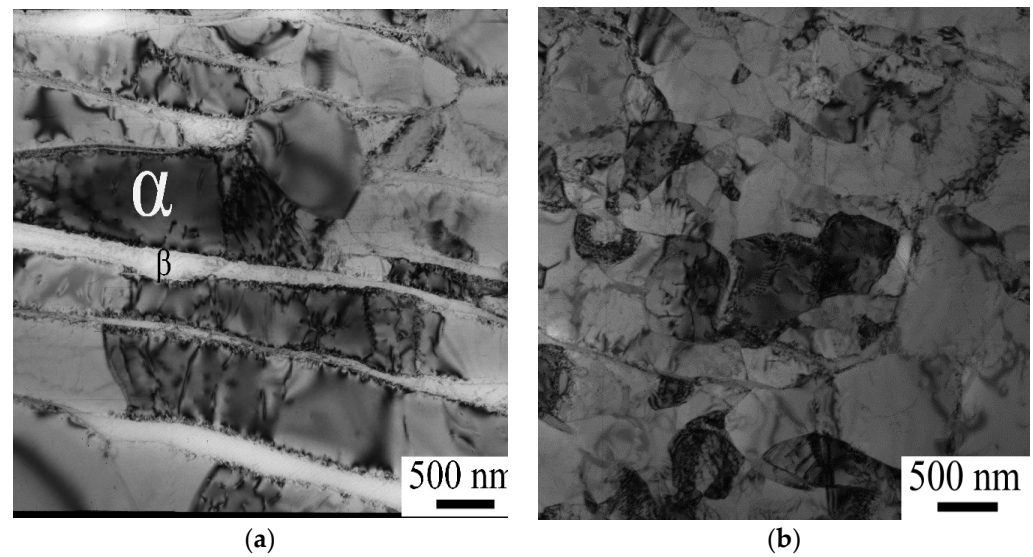


Figure 15. TEM images of the SPS-Alloy after deformation at 900 °C (a) or 950 °C (b).

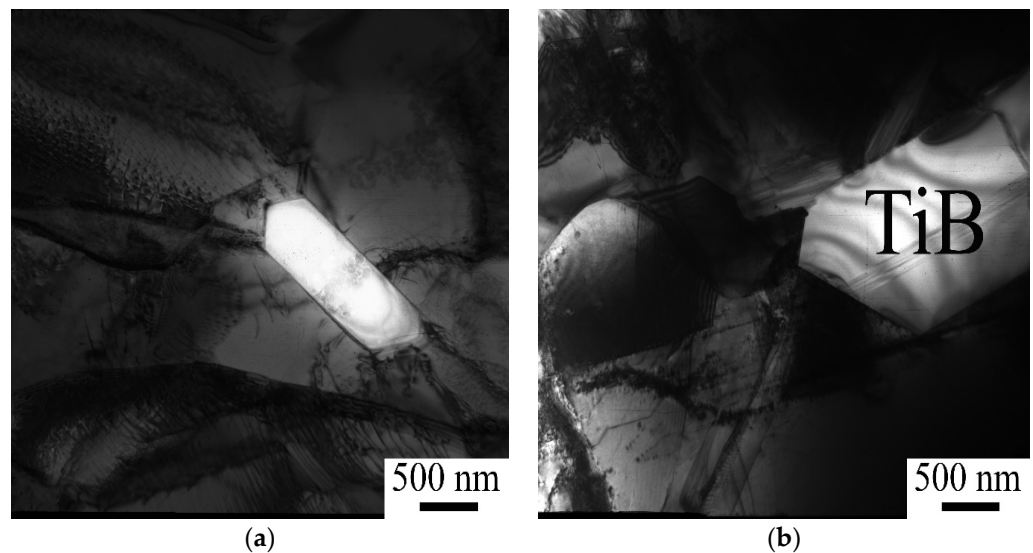


Figure 16. TEM images of the TiB particles in the SPS-Composite (a,b) strained at 900 °C (a) or 950 °C (b).

4. Discussion

The obtained results clearly show different structures and mechanical behaviors of the Ti_{6.5}Al-2Zr-1Mo-1V/TiB composite obtained by vacuum arc melting and spark plasma sintering. The main difference in the microstructure is associated with either a relatively homogeneous (in the case of the AC-Composite) or a more regular (produced by SPS) distribution of the reinforcements. This distribution results not only in different mechanical properties but also in different structure responses to hot deformation.

The difference in the structure of the AC-Composite and SPS-Composite is also indicated by the results of modeling within the dynamic material model (DMM). Based on this model and flow stress Arrhenius dependence, the power dissipation efficiency and instability diagrams depending on the temperature, strain rate, and deformation were constructed (Figure S3). It was shown that for the AC-Composite, an expansion of the deformation instability region to higher temperatures is observed compared to the SPS-Composite, which confirms different structure responses to hot deformation for both composites.

The main contribution of homogeneously distributed TiB fibers to the strength is associated with the load transfer mechanism, the efficiency of which is lower than that

of Orowan strengthening [26], particularly in the case of coarse TiB particles (~2.6 μm in diameter, ~26 μm in length). In contrast, the network-like distribution of TiB creates a tough framework filled with a ductile Ti-6.5Al-2Zr-1Mo-1V matrix. At room temperature, this structure provides a noticeably higher strength (Table 1) in comparison to the AC-Composite. Similar benefits in strength due to the formation of the network architecture in MMCs were early reported in [18,25]. In addition, the Ti-6.5Al-2Zr-1Mo-1V alloy obtained by SPS also shows a higher strength at room temperature in comparison to the as-cast condition, which can stem from a higher level of impurities proper for powder materials [9,11]. Therefore, the overall strength of the SPS-Composite is a superposition of the strength characteristic of the matrix and the network-like architecture of TiB.

More interesting is that, at elevated temperatures (above 400 °C), the AC-Composite with the relatively homogeneously distributed TiB fibers becomes stronger than the SPS-Composite with the network-like architecture. The difference reached almost 50% at 800 and 900 °C. Since the strength of the SPS-Alloy compared to AC-Alloy remained higher at almost all studied temperatures (Table 1), it may be concluded that at elevated temperatures, the homogeneous distribution of the reinforcements in the composite structure may be more preferable than the network-like architecture. At the same time, Huang and co-authors reported better high-temperature behavior of a TiBw/Ti6Al4V composite with a network architecture at elevated temperatures in comparison with counterparts with randomly distributed reinforcements [18,25]. Therefore, this point requires a more careful examination. Another intriguing feature observed in the composites obtained by different methods is associated with different globularization kinetics during hot deformation. The analysis of activation energy, Q , (Figure 17) obtained for the as-cast or as-sintered composites compressed in the interval of 750–950 °C suggests marginal variations in the controlling deformation mechanisms. It should be noted that earlier reported values of Q and the stress exponent, n , for the similar temperature interval for TiB-reinforced composites with a single-phase hcp Ti matrix ($n \sim 7$; $Q = 168$ kJ/mol) [19] or bcc Ti-15Mo matrix ($n \sim 5$; $Q = 241$ kJ/mol) [27] were found to be considerably lower than the values of Q obtained in the present work ($n \approx 4.6\text{--}5.2$; $Q \approx 350\text{--}410$ kJ/mol; Figure 13). Self-diffusion in α Ti with $Q = 150$ kJ/mol [28] can therefore be hardly considered as a controlling mechanism of deformation. Dislocation slip along prismatic planes with thermally activated overcoming of solute atoms ($Q = 250\text{--}330$ kJ/mol) is more likely to be understood as the main mechanism of rate control [29]. Some increase in Q can be expected due to the development of dynamic recrystallization/globularization [30]. In addition, greater values of Q and n , in the case of the composite, can be associated with the inhibition of dislocation movement by the TiB particles [25].

Meanwhile, the values of Q and n in the case of the as-cast condition are noticeably higher than those for the SPS-Composite (Figure 17). Since all other parameters of the chemical composition and microstructure are similar, the main reason for the difference in the activation parameters, as well as in the globularization kinetics, can be associated with different distributions of the TiB particles. Specifically, a rather homogeneous reinforcements distribution in the AC-Composite resulted in more intensive involvement of the Ti-based matrix into plastic flow and thus in more pronounced globularization (Figure 11a). In contrast, at the early stages of plastic strain, the network-like architecture constrains the deformation of the matrix, thereby postponing the onset of globularization (Figures 9 and 11a).

In addition to temperature, strain rate, strain degree, and boride content, the method of composite production can also affect the deformation behavior of metal matrix composites. Studying the deformation behavior and structure evolution of metal matrix composites can help optimize the thermomechanical processing parameters. To reduce time and resource costs, the deformation behavior in a wide range of temperatures and rates was modeled using a phenomenological model for the flow stress based on the Arrhenius dependence. The results of the deformation behavior modeling were displayed as process maps (within the dynamic material model) displaying the efficiency of power dissipation and areas of unstable deformation. Based on the process maps, it was shown that for the cast metal

matrix composite, an expansion of the instability zone to higher temperatures is observed compared to the SPS composite.

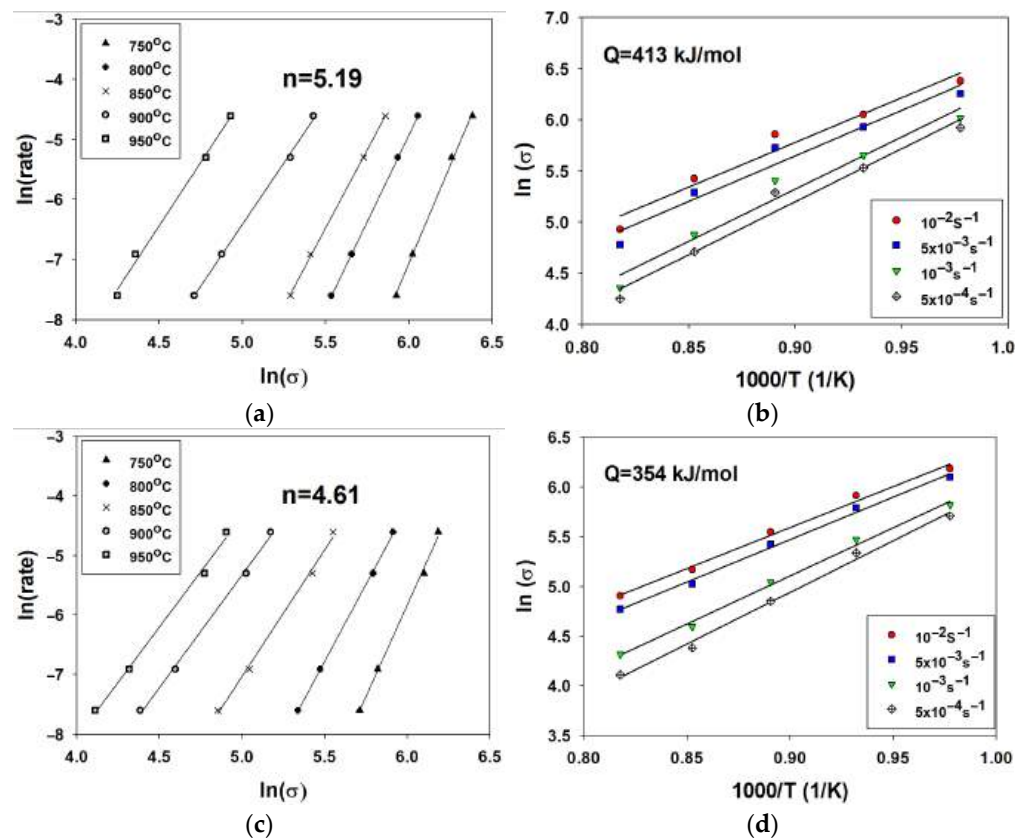


Figure 17. Dependence of the strain rate on stress on a logarithmic scale (a,c) and the semi-logarithmic Arrhenius plot of the steady-state flow stress on the reciprocal temperature (b,d) for the AC- (a,b) and SPS-Composites (c,d) compressed in the range $T = 750\text{--}950\text{ }^{\circ}\text{C}$.

5. Conclusions

The effect of deformation in the interval of 20–950 °C on the structure and properties of the Ti-6.5Al-2Zr-1Mo-1V/TiB composite obtained by vacuum arc melting or spark plasma sintering was investigated. The conclusions are as follows:

1. The initial microstructure of the unreinforced Ti-6.5Al-2Zr-1Mo-1V alloy in the as-cast and as-sintered conditions was quite typical and consisted of colonies of α -lamellae in the β matrix. The microstructure of the as-cast Ti-6.5Al-2Zr-1Mo-1V/TiB composite consisted of TiB fibers randomly distributed within the two-phase α/β matrix. The as-sintered composite had a network-like microstructure, in which areas of the two-phase α/β matrix were delineated by walls of TiB fibers. It was shown that the volume fraction of the β phase in the structure of both composites was $\sim 6\%$. The volume fraction of TiB was found to be $\sim 10\%$ and 6% in the as-cast and as-sintered conditions, respectively.
2. Alloying with 3 wt.% TiB₂ as a reinforcing component of the initial Ti-6.5Al-2Zr-1Mo-1V alloy charge had a significant effect on the mechanical properties of the Ti-6.5Al-2Zr-1Mo-1V/TiB composites compared to the unreinforced alloys. At room temperature, the yield strength of the as-cast and as-sintered Ti-6.5Al-2Zr-1Mo-1V alloy were 800 and 915 MPa, respectively, while the plasticity was 18% for both conditions. The addition of TiB fibers contributed to a ~ 40 and 50% strength increment, with the values of 1100 and 1370 MPa for the as-cast and as-sintered composites, respectively, without a visible drop in plasticity. In the as-sintered composite, the strengthening effect reduced during compression at 400 °C and almost disappeared at elevated

temperatures of 800–950 °C. The as-cast composite showed much higher strength properties during warm and hot deformation: at 800–950 °C, the yield strength of the as-cast composite was twice as high as that of the unreinforced condition.

3. A higher rate and degree of globularization was established for the as-cast composite compared to the unreinforced alloy. It was shown that the fraction of the globularized structure increased with increasing deformation temperature in the interval of 800–950 °C from ~40 to ~80% in the unreinforced alloy and from ~55 to ~90% in the composite. The main qualitative difference in the microstructure evolution during hot deformation of the as-cast and as-sintered states is a noticeably lower rate and degree of globularization of the α -lamellae. This trend is typical for both the as-sintered composite and the unreinforced as-sintered alloy. For the as-sintered condition, the volume fraction of globular α increased from ~37 to ~52% in the unreinforced alloy and from ~37 to ~56% in the composite. During uniaxial hot compression of the as-cast composite, TiB fibers reoriented towards the metal flow direction. A significant shortening of the TiB fibers from ~25 μm in the initial state to ~5–7 μm after hot compression was shown. The network microstructure formed in the composite produced by SPS transformed into clusters of borides unevenly distributed within the matrix. The shortening of TiB fibers was less intensive in comparison to that of the as-cast composite.
4. The calculated activation energy of plastic deformation Q was found to be 413 kJ/mol for the as-cast composite and 354 kJ/mol for the as-sintered composite, which suggests that there was no change in the control mechanism of deformation, which is dislocation slip along prismatic planes with thermally activated overcoming of solute atoms.
5. Based on the simulation within the framework of the dynamic material model, it is shown that for the as-cast composite, an expansion of the deformation instability region towards higher temperatures is observed compared to the as-sintered composite, which confirms the different responses of the structure to hot deformation for both composites.

Supplementary Materials: The following supporting information can be downloaded at <https://www.mdpi.com/article/10.3390/met14121337/s1>, Figure S1: Liner fittings: $\ln(\sigma) - \ln(\dot{\epsilon})$ (a), $\sigma - \ln(\dot{\epsilon})$ (b), $\ln[\sinh(\alpha\sigma)] - \ln(\dot{\epsilon})$ (c) and $\ln[\sinh(\alpha\sigma)] - 1000/T$ (d) for AC-composites; Figure S2: Liner fittings: $\ln(\sigma) - \ln(\dot{\epsilon})$ (a), $\sigma - \ln(\dot{\epsilon})$ (b), $\ln[\sinh(\alpha\sigma)] - \ln(\dot{\epsilon})$ (c) and $\ln[\sinh(\alpha\sigma)] - 1000/T$ (d) for SPS-composites; Figure S3: Strain-dependence graphs for α (a), n (b), Q (c) and $\ln(A)$ (d) for AC-composite; Figure S4: Strain-dependence graphs for α (a), n (b), Q (c) and $\ln(A)$ (d) for SPS-composite; Figure S5: Processing maps for AC-composite at strain $\epsilon = 0.1$ (a), $\epsilon = 0.4$ (b) and for SPS-composite at strain $\epsilon = 0.1$ (c), $\epsilon = 0.4$ (d). The grey shaded areas indicate unstable areas and the remaining parts are safe areas; Table S1: Coefficients of 5th degree polynomials for interpolation of α , n , Q and $\ln(A)$ of AC and SPS-composites.

Author Contributions: Conceptualization, M.O. and V.S.; methodology, M.O., I.A., V.S. and D.K.; validation, M.O., V.S. and S.Z. (Sergey Zherebtsov); formal analysis, M.O., D.K., N.Y., S.Z. (Shiyan Zhao), L.H. and S.Z. (Sergey Zherebtsov); investigation, M.O., I.A., V.S., D.K., N.S., N.Y., S.Z. (Shiyan Zhao) and L.H.; resources, M.O., V.S., N.S. and S.Z. (Sergey Zherebtsov); data curation, M.O., V.S., N.S., N.Y., L.H. and S.Z. (Sergey Zherebtsov); writing—original draft, M.O., V.S. and D.K.; writing—review and editing, N.S., N.Y., L.H. and S.Z. (Sergey Zherebtsov); visualization, M.O., I.A., V.S. and S.Z. (Shiyan Zhao); supervision, M.O., V.S. and S.Z. (Sergey Zherebtsov); project administration, V.S.; funding acquisition, V.S. All authors have read and agreed to the published version of the manuscript.

Funding: This research was funded by the Russian Science Foundation, Grant Number 23-49-00108.

Data Availability Statement: The original contributions presented in the study are included in the article/Supplementary Material, further inquiries can be directed to the corresponding author.

Acknowledgments: The authors gratefully acknowledge the financial support from the Russian Science Foundation (Grant Number 23-49-00108). A part of this research (SEM characterization) was partially funded by the Ministry of Science and Higher Education of the Russian Federation as part of the World-Class Research Center program: Advanced Digital Technologies (Contract no. 075-15-2022-312 dated 20 April 2022). The authors are grateful to the personnel of the Joint Research Centre, Belgorod State National Research University, for their assistance with the instrumental analysis.

Conflicts of Interest: The authors declare no conflicts of interest.

References

1. Williams, J.C.; Boyer, R.R. Opportunities and Issues in the Application of Titanium Alloys for Aerospace Components. *Metals* **2020**, *10*, 705. [[CrossRef](#)]
2. Pushp, P.; Dasharath, S.M.; Arati, C. Classification and applications of titanium and its alloys. *Mater. Today* **2022**, *54*, 537–542. [[CrossRef](#)]
3. Veiga, C.; Davim, J.P.; Loureiro, A.J.R. Properties and applications of titanium alloys: A brief review. *Rev. Adv. Mater. Sci.* **2012**, *32*, 14–34.
4. Sun, Q.J.; Xie, X. Microstructure and mechanical properties of TA15 alloy after 433 thermo-mechanical processing. *Mater. Sci. Eng. A* **2004**, *724*, 493–501. [[CrossRef](#)]
5. Sun, Z.; Yang, H. Microstructure and mechanical properties of TA15 titanium alloy 436 under multi-step local loading forming. *Mater. Sci. Eng. A* **2009**, *523*, 184–192. [[CrossRef](#)]
6. Tabie, V.M.; Li, C.; Saifu, W.; Li, J.; Xu, X. Mechanical properties of near alpha titanium alloys for high-temperature applications—A review. *Aircr. Eng. Aerosp. Technol.* **2020**, *92*, 521–540. [[CrossRef](#)]
7. Zharebtsov, S.V.; Salishchev, G.A.; Galejev, R.M.; Valiakmetov, O.R.; Mironov, S.Y.; Semiatin, S.L. Production of submicrocrystalline structure in large-scale Ti–6Al–4V billet by warm severe deformation processing. *Scripta Mater.* **2004**, *51*, 1147–1151. [[CrossRef](#)]
8. Weiss, I.; Semiatin, S.L. Thermomechanical processing of alpha titanium alloys—An overview. *Mater. Sci. Eng. A* **1999**, *263*, 243–256. [[CrossRef](#)]
9. Hayat, M.D.; Singh, H.; He, Z.; Cao, P. Titanium metal matrix composites: An overview. *Compos. Part A Appl. Sci. Manuf.* **2019**, *121*, 418–438. [[CrossRef](#)]
10. Shetty, R.; Hegde, A.; Shetty SV, U.K.; Nayak, R.; Naik, N.; Nayak, M. Processing and Mechanical Characterisation of Titanium Metal Matrix Composites: A Literature Review. *J. Compos. Sci.* **2022**, *6*, 388. [[CrossRef](#)]
11. Morsi, K. Review: Titanium–titanium boride composites. *J. Mater. Sci.* **2019**, *54*, 6753–6771. [[CrossRef](#)]
12. Sharma, D.K.; Mahant, D.; Upadhyay, G. Manufacturing of metal matrix composites: A state of review. *Mater. Today Proc.* **2020**, *26*, 506–519. [[CrossRef](#)]
13. Casati, R.; Vedani, M. Metal Matrix Composites Reinforced by Nano- Particles—A review. *Metals* **2014**, *4*, 65–83. [[CrossRef](#)]
14. Zhang, C.J.; Kong, F.T.; Xu, L.J.; Zhao, E.T.; Xiao, S.L.; Chen, Y.Y.; Deng, N.J.; Ge, W.; Xu, G.J. Temperature dependence of tensile properties and fracture behavior of as rolled TiB/Ti composite sheet. *Mater. Sci. Eng. A* **2012**, *556*, 962–969. [[CrossRef](#)]
15. Fröhlich, M.; Braun, R.; Leyens, C. Oxidation resistant coatings in combination with thermal barrier coatings on γ -TiAl alloys for high temperature applications. *Surf. Coat. Technol.* **2006**, *201*, 3911–3917. [[CrossRef](#)]
16. Lin, J.; Stinnett, T.C. Development of thermal barrier coatings using reactive pulsed dc magnetron sputtering for thermal protection of titanium alloys. *Surf. Coat. Technol.* **2020**, *403*, 126377. [[CrossRef](#)]
17. Thakare, J.G.; Pandey, C.; Mahapatra, M.M.; Mulik, R.S. Thermal Barrier Coatings—A State of the Art Review. *Met. Mater. Int.* **2021**, *27*, 1947–1968. [[CrossRef](#)]
18. Huang, L.; An, Q.; Geng, L.; Wang, S.; Jiang, S.; Cui, X.; Zhang, R.; Sun, F.; Jiao, Y.; Chen, X.; et al. Multi-scale Architecture and Superior High-temperature Performances of Discontinuously Reinforced Titanium Matrix Composites. *Adv. Mater.* **2021**, *33*, 2000688. [[CrossRef](#)]
19. Ozerov, M.; Klimova, M.; Kolesnikov, A.; Stepanov, N.; Zharebtsov, S. Deformation behavior and microstructure evolution of a Ti/TiB metal-matrix composite during high-temperature compression tests. *Mater. Des.* **2016**, *112*, 17–26. [[CrossRef](#)]
20. Zener, C.; Hollomon, J.H. Effect of strain rate upon plastic flow of steel. *Br. J. Appl. Phys.* **1944**, *15*, 22–32. [[CrossRef](#)]
21. Katoch, S.; Chauhan, S.S.; Kumar, V. A review on genetic algorithm: Past, present, and future Multimed. *Tools Appl.* **2021**, *80*, 8091–8126. [[CrossRef](#)] [[PubMed](#)]
22. Xia, Y.; Shu, X.; Zhang, Q.; Pater, Z.; Li, Z.; Xu, H.; Xu, C. Modified Arrhenius constitutive model and simulation verification of 2A12-T4 aluminum alloy during hot compression. *J. Mater. Res. Technol.* **2023**, *26*, 1325–1340. [[CrossRef](#)]
23. Prasad, Y.; Gegel, H.; Doraivelu, S.; Malas, J.; Morgan, J.; Lark, K.; Barker, D. Modeling of dynamic material behavior in hot deformation: Forging of Ti-6242. *Metall. Trans. A* **1984**, *15*, 1883–1892. [[CrossRef](#)]
24. Prasad, Y.; Seshacharyulu, T. Processing maps for hot working of titanium alloys. *Mater. Sci. Eng. A* **1998**, *243*, 82–88. [[CrossRef](#)]
25. Zhang, Y.; Huang, L.; Liu, B.; Geng, L. Hot deformation behavior of in-situ TiBw/Ti6Al4V composite with novel network reinforcement distribution. *Trans. Nonferrous Met. Soc. China* **2012**, *22*, 465–471. [[CrossRef](#)]

26. Chen, B.; Shen, J.; Ye, X.; Jia, L.; Li, S.; Umeda, J.; Takahashi, M.; Kondoh, K. Length effect of carbon nanotubes on the strengthening mechanisms in metal matrix composites. *Acta Mater.* **2017**, *140*, 317–325. [[CrossRef](#)]
27. Zherebtsov, S.; Ozerov, M.; Klimova, M.; Moskovskikh, D.; Stepanov, N.; Salishchev, G. Mechanical behavior and microstructure evolution of a Ti-15Mo/TiB titanium–matrix composite during hot deformation. *Metals* **2019**, *9*, 1175. [[CrossRef](#)]
28. Frost, H.J.; Ashby, M.F. *Deformation-Mechanism Maps*; Pergamon Press: Oxford, UK, 1982; pp. 1–166.
29. Conrad, H. Effect of interstitial solutes on the strength and ductility of titanium. *Prog. Mater. Sci.* **1981**, *26*, 123–403. [[CrossRef](#)]
30. Raj, S.V.; Langdon, T.G. Creep behavior of copper at intermediate temperatures—I. Mechanical characteristics. *Acta Metall.* **1989**, *37*, 843–852. [[CrossRef](#)]

Disclaimer/Publisher’s Note: The statements, opinions and data contained in all publications are solely those of the individual author(s) and contributor(s) and not of MDPI and/or the editor(s). MDPI and/or the editor(s) disclaim responsibility for any injury to people or property resulting from any ideas, methods, instructions or products referred to in the content.